Proceedings of the 11th ICPMG 2026
11th International Conference on Physical Modelling in Geotechnics
8-12 June 2026, Zurich, Switzerland


# Simulation system for wind, wave, and seismic loading in centrifuge testing of offshore wind turbines

H. Takahashi
*Tokyo University of Marine Science and Technology, Tokyo, Japan, takahashi-h@kaiyodai.ac.jp*

T. Tsuchida
*Ecoh, Tokyo, Japan, t-tsuchida@ecoh.co.jp*

H. Kashima, Y. Ohya, O. Kurihara
*Port and Airport Research Institute, Yokosuka, Japan, kashima-h2w7@p.mpat.go.jp, ooya-y@p.mpat.go.jp, kurihara-oo@p.mpat.go.jp*

T. Ichikawa
*GeoDesign, Tokyo, Japan, ichikawa@geodesign.co.jp*

**ABSTRACT:** Fixed-bottom offshore wind turbines experience complex displacement and vibration under simultaneous wind, wave, and seismic loading, driven by coupled aerodynamic, hydrodynamic, and geotechnical interactions. To investigate these multi-physics responses, the authors developed a centrifuge-based experimental apparatus capable of applying all three external forces within a centrifugal field. This paper reviews the relevant similitude laws, describes the apparatus design, and presents initial validation tests. Results confirm that the system can reproduce wind, wave, and seismic forces, inducing horizontal displacement and vibration in the model turbine.

## 1 INTRODUCTION

In recent years, the global deployment of offshore wind turbines has advanced considerably. In fixed-bottom systems, blades rotate under wind action, while submerged components are subjected to wave and current forces, inducing displacement and vibration in the tower and foundation. The entire structure is stabilised by subgrade reaction forces. During seismic events, vibrations from the seabed and seawater are transmitted to the turbine, causing further motion. Thus, offshore wind turbines respond to forces from three domains: air, water, and ground. Understanding these interactions is essential for sound structural design (see Figure 1).

Extensive research on wind turbine behaviour under wind, wave, and current loads has been conducted in aerodynamics and coastal engineering, yielding mature design methodologies. In geotechnical engineering, ground response has been studied through full-scale and centrifuge model tests capable of replicating prototype stress conditions. However, most regions deploying offshore turbines have experienced limited seismic activity, resulting in insufficient consideration of earthquake effects. Reported seismic damage to wind turbines underscores the need to account for earthquake loading (e.g. Wang & Ishihara, 2024). In particular, the combined influence of aerodynamic and hydrodynamic forces with seismic ground motion remains largely unexplored (e.g. Yang et al., 2020).

Current Japanese design guidelines (Exploratory Committee for Offshore Wind Power Facilities, 2020) adopt separate elastic analyses for aerodynamic/wave loading and seismic response, combining peak values from each to estimate total external force. This approach overlooks the interaction among aerodynamic, hydrodynamic, and geotechnical forces. To address this gap, it is essential to apply wind, wave,

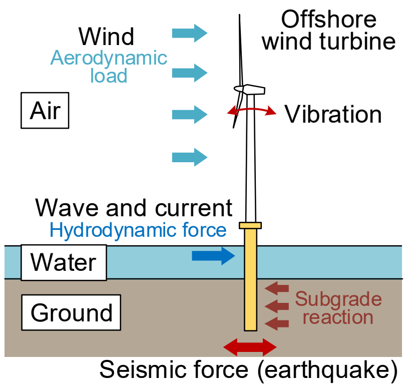


*Figure 1. Bottom-fixed offshore wind turbine subjected to three external forces.*

and seismic forces simultaneously to offshore wind turbine models inclusive of ground conditions, enabling a more accurate assessment of multi-physics response.

In geotechnical engineering, centrifugal model testing has been employed to replicate the stress states of full-scale structures by applying centrifugal forces to scaled models (Taylor, 1995). Model tests incorporating wave loading, in addition to seismic excitation, have also been conducted (Sekiguchi & Phillips, 1991; Baba et al., 2002; Takahashi et al., 2019; Takahashi et al., 2022). Research on wave–ground interaction is advancing, with the current state summarised by the Research Committee of the Japan Society of Civil Engineers (Arikawa, 2024). In contrast, wind-loading tests have yet to be realised within centrifugal fields.

We hypothesised that applying wind, wave, and seismic forces simultaneously to offshore wind turbine models incorporating ground would enable investigation of turbine responses that reflect the combined and interacting effects of subgrade reaction forces under multi-physics loading. Over the past two years, the authors developed a simulator capable of generating wind, wave, and seismic forces concurrently within a centrifugal field. This paper presents the relevant similitude laws, outlines the development of the wind–wave–seismic environment simulator, and reports on a series of validation tests. An overview of the apparatus has been published previously (Takahashi et al., 2025). Here, we further describe the apparatus and present new experimental results highlighting the influence of ground conditions on turbine response characteristics.

## 2 SIMILARITY LAW

### 2.1 Similitude in water, ground, and structure

In centrifuge model tests, the application of downward centrifugal force elevates stress and pore water pressure within the ground, thereby replicating the conditions present in full-scale structures. This enables reproduction of deformation and failure behaviour at prototype scale. Water-related tests can also be conducted in accordance with the Froude law, with similarity ratios for physical quantities—including structural components—summarised in Table 1. Adherence to the Froude law yields the advantage that flow velocity similarity becomes unity, due to cancellation between dimensional and gravitational acceleration ratios—consistent with ground velocity scaling. However, because a viscous fluid was not used in the present tests, the seepage time becomes

*Table 1. Similarity ratios (model/prototype).*

*(a) Water and ground*

| Physical value | Water | Ground |
|---|---|---|
| Length | $1/N$ | $1/N$ |
| Density | 1 | 1 |
| Strain | 1 | 1 |
| Gravitational acceleration | $N$ | $N$ |
| Kinematic viscosity | 1 | 1 |
| Time (dynamic) | $1/N$ | $1/N$ |
| Time (seepage) | — | $1/N^2$ |
| Stress, Water pressure | 1 | 1 |
| Tangent stiffness | 1 | 1 |
| Hydraulic conductivity | — | $N$ |
| Displacement | $1/N$ | $1/N$ |
| Velocity | 1 | 1 |
| Acceleration | $N$ | $N$ |

*(b) Structure*

| Physical value | Structure |
|---|---|
| Mass | $1/N^3$ |
| Force | $1/N^2$ |
| Displacement | $1/N$ |
| Moment | $1/N^3$ |
| Angle of inclination | 1 |
| Deformation modulus | 1 |

$1/N^2$ of that in the prototype. When phenomena such as soil liquefaction are to be reproduced, the use of a viscous fluid is required. Certain phenomena, such as scouring at the water–ground interface, remain outside the scope of established similarity laws, indicating limitations in the universal applicability of centrifugal modelling. Similarity ratios for structures such as wind turbines are consistent with those for water and ground, with structure-specific ratios detailed in Table 1(b). For details on the similarity ratios of soil, water, and structures, the reader is referred to Arikawa (2024).

### 2.2 Similitude in wind and wind forces

In model tests involving a single wind turbine and its surroundings, the scale is sufficiently small to allow gravity's influence on wind to be effectively neglected. Wind similitude laws within a centrifugal field remain consistent with those in a gravitational field. To accurately replicate the airflow around turbine blades, the Reynolds number must match that of the prototype structure due to the dominant role of viscosity. However, installing a high-speed wind tunnel within the centrifugal testing apparatus is impractical. Thus, as in conventional wind tunnel tests under gravity, a low-speed tunnel was employed, operating in the low Reynolds number regime.

The developed simulator is designed to apply three external forces—wind, waves, and seismic motion—to a rotating-blade wind turbine model to investigate vibrational response. Reproducing detailed airflow around blades or evaluating power generation and control strategies was not the objective. Only thrust force was simulated; other turbine characteristics, such as tip speed ratio, were not reproduced. Accordingly, similarity rules were relaxed to permit low Reynolds number testing, and model parameters were adjusted to match thrust force. The force similarity ratio is $1/N^2$, and turbine loads must conform to this scaling. The thrust force $F_x$ is expressed by the following equation.

$$F_x = \frac{1}{2} C_T \rho U^2 A \quad (1)$$

Here, $C_T$: thrust coefficient, $\rho$: air density, $U$: wind tunnel velocity, $A$: rotor swept area. Due to the limited cross-sectional area of the simulator's wind tunnel, blade length must be reduced. Scaling down the actual turbine results in a low tip speed ratio and, consequently, a reduced thrust coefficient. Moreover, the rotor area is smaller than the geometric similarity ratio of $1/N^2$. Given that air density and wind speed similarity ratios are unity, the resulting thrust force ratio falls below $1/N^2$.

To address this, blade width was increased in subsequent tests to achieve a higher thrust coefficient under low tip speed conditions. This leverages the characteristic that increased solidity (blade area/rotor area) enhances thrust at low tip speeds. Although the setup cannot replicate fine-scale vibrations from wind turbulence due to Reynolds number mismatch, it is deemed suitable for investigating turbine vibration and stress responses under subgrade reaction forces, incorporating aerodynamic, wave, and seismic effects. The apparatus also enables reproduction of interactions among these three external forces.

## 3 SIMULATOR DEVELOPMENT

### 3.1 Wave generator and shaking table

The centrifuge housing the simulator is owned by the Port and Airport Research Institute (PARI). The overall configuration of the apparatus and platform is shown in Figure 2; for further details, refer to Takahashi et al. (2019). The platform measures 1.7 m × 1.6 m and supports up to 2.7 ton. This system is actively used for model tests integrating ground effects with wave loading (Takahashi et al., 2019; 2022).

Due to spatial constraints, a long wave flume cannot be installed on the centrifuge platform. Instead of transforming offshore waves into shallow-water waves, near-field waves are reproduced using a piston-type wave-making plate (Figure 3(a)). Although wave-absorbing materials are placed along the walls, some reflection remains. Accordingly, the results must be evaluated under the combined action of incident and reflected waves. The wave generator is mounted on a support frame spanning the shaking table and specimen container, with only the plate suspended into the container from above. As the plate remains stationary during container vibration, waves are generated by the motion itself. However, seismic vibrations are high-frequency and low-amplitude (several millimetres), causing wave energy to dissipate before reaching the structure. The wave-making plate is driven unidirectionally by a hydraulic cylinder, capable of displacements up to ±110 mm (±5.5 m at 50$g$), with a drive force of 8100 N and operating frequencies between 0.5–10 Hz (0.01–0.2 Hz at 50$g$).

For seismic simulation, an existing shaking table predating the simulator's development was repurposed (Figure 3(b)). This table also operates unidirectionally via hydraulic actuation, with a maximum amplitude of ±10 mm (±0.5 m at 50$g$), a thrust capacity of 386 kN, and vibration frequencies up to 150 Hz (3 Hz at 50$g$).

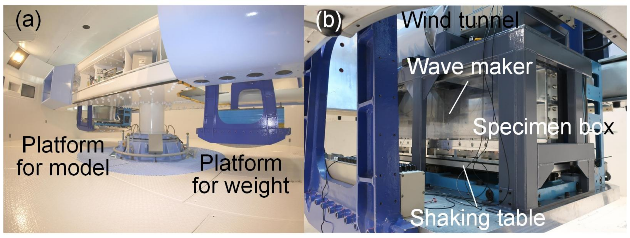

*Figure 2. Centrifuge testing apparatus and platform.*

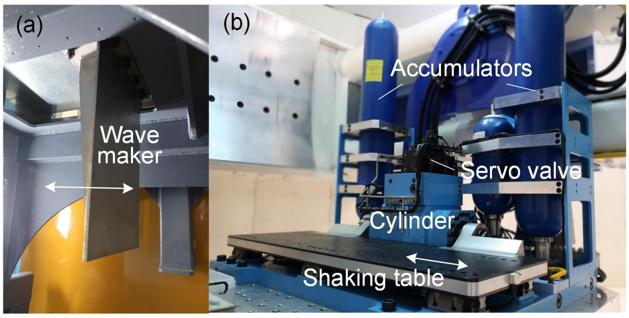

*Figure 3. Wave generator and shaking table.*

### 3.2 Wind tunnel blower

Installing a blower and wind tunnel within the centrifuge was unprecedented and posed the greatest challenge in developing the simulator. The platform had to accommodate the blower, wind tunnel, wave generator, shaking table, model, and camera systems, making the installation of large components impractical. Consequently, an open-type (Eiffel-type) wind tunnel with open intake and exhaust was adopted.

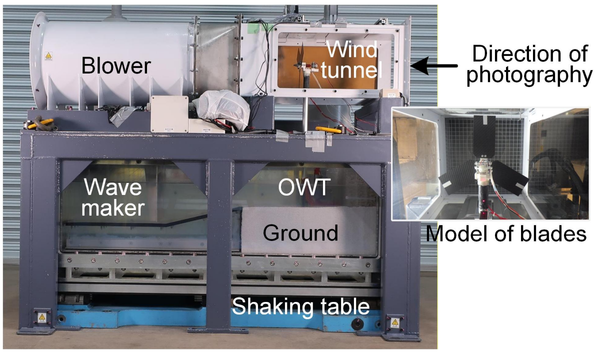


*Figure 4. Developed simulator (photographed outside centrifuge).*

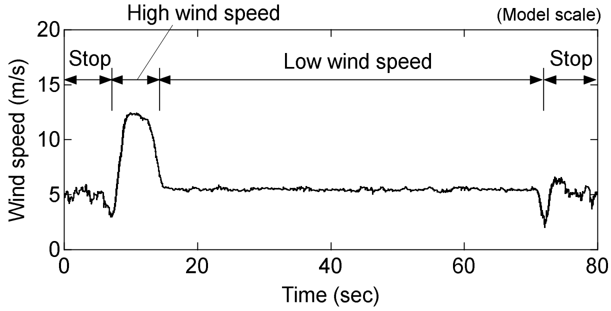


*Figure 5. Time histories of measured wind speed.*

*Table 2. Average wind speed and coefficient of variation in the wind tunnel.*

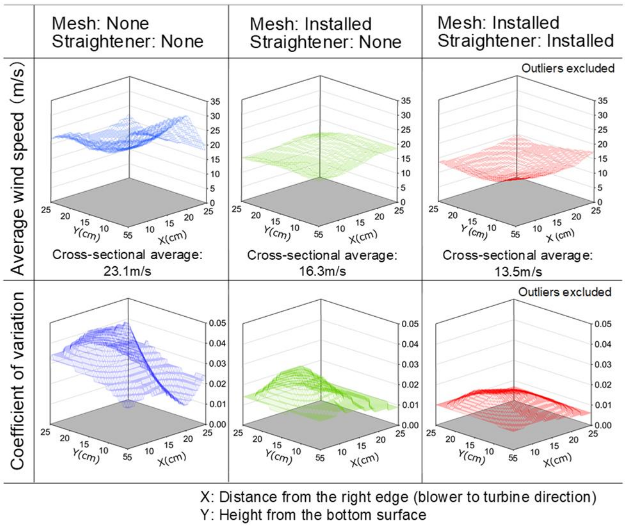


Both the blower and tunnel were mounted atop the support frame (see Figure 4), with wind direction aligned to wave propagation and vibration axes. A fan-type blower with a high-capacity motor was selected to operate under centrifugal conditions and generate strong airflow. The fan diameter was approximately 350 mm, and motor speed was remotely controlled from the centrifuge control room.

The wind tunnel's internal dimensions are 300 mm × 300 mm, with a length of 730 mm. The rotor of the wind turbine model is installed within this tunnel. As a full-scale wind tunnel supplying air to the entire turbine was infeasible, airflow was directed solely at the rotor, excluding the tower. Moreover, due to limited spacing between blower and model, conventional components such as diffuser, rectifier, or converging sections could not be incorporated, making uniform flow rectification difficult. To mitigate planar and temporal turbulence, a wire mesh and rectifying grid (15 mm × 15 mm) were installed between the blower and tunnel. Table 2 presents 3D surface plots of wind speed standard deviation normalised by mean speed, along with mean wind speed measured via Pitot tube in a gravitational field. The mesh reduced spatial variation and coefficient of variation, while the rectifying grid further improved flow uniformity.

Preliminary experiments were conducted to assess wind conditions within the centrifugal field. A hot-wire anemometer was used for its stable readings. Figure 5 shows wind speeds measured in a 50$g$ field without the turbine installed. Measurements were taken 22 mm below the tunnel ceiling and 89 mm from the left wall, viewed from the fan toward the turbine. The data span the blower's off–on–off cycle. Initially, motor speed was increased, then reduced and stabilised. Wind persisted during blower inactivity due to the centrifuge's cooling airflow, which moves from tunnel to blower and was likely detected by the sensor. Upon blower activation, this flow reversed, reducing fluctuations and enabling stable wind generation.

# 4 TEST CONDITIONS

## 4.1 Wind turbine model

Figure 6 (right) presents cross-sectional views of the blades, hub, and nacelle (hereafter RNA) of the wind turbine model used in the model tests. For the 50$g$ centrifugal field, a 1/50 scale model was adopted, representing a 75–100 kW turbine. Assuming an RNA mass of 5 ton and a tower/foundation pile mass of 10 ton, the mass similarity ratio of $1/N^3$ yields model masses of 40 g and 80 g, respectively. This required a highly lightweight design, prompting mass reduction across components. Blades were constructed from 1.5 mm thick carbon fibre reinforced plastic sheets; the nacelle was 3D-printed in resin, and the rotor hub fabricated from aluminium. Mechanical components were minimised, with only an ultra-compact motor installed. These measures reduced blade mass to 81 g and hub/nacelle to 73 g. For the tower and foundation pile, 1.0 mm thick aluminium cylindrical pipes were used, yielding a mass of 146 g—intentionally heavier than the RNA to suppress excessive vibration, despite the availability of thinner alternatives.

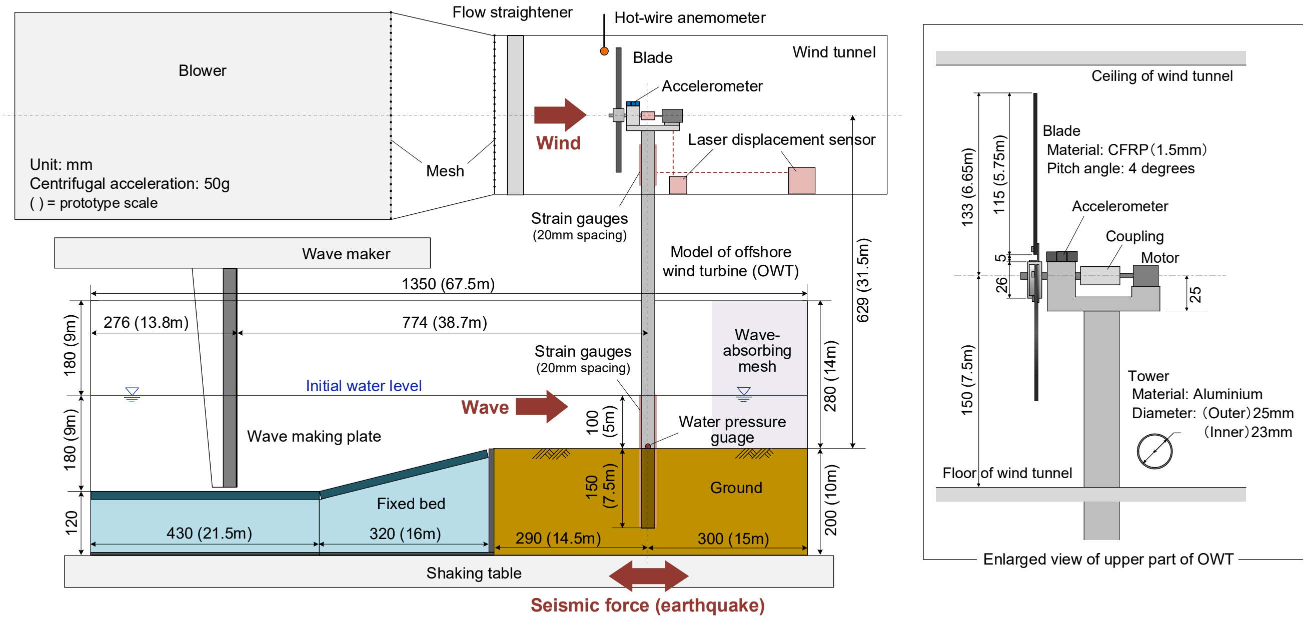


*Figure 6. Cross-section of the wind turbine model and overall model setup.*

To assess turbine vibrations, three ultra-compact accelerometers were mounted on the nacelle in orthogonal directions. Vertical displacement of the nacelle and horizontal displacement of the tower section beneath it were measured using laser displacement sensors. Strain gauges were affixed to the cylindrical pipe simulating the tower and foundation to capture bending strain. The blade pitch angle was fixed at 4 degrees prior to testing. Since motor voltage and current increase with rotational speed, their relationship was examined in advance, and rotational speed was estimated from voltage and current readings.

## 4.2 Models and testing procedure

A cross-sectional view of the model is shown in Figure 6 (left), with bracketed dimensions indicating prototype scale equivalents. The left side of the specimen container housed the wave-generating section, where a fixed bed was secured. The right side served as the ground section, into which the wind turbine model was embedded. Gifu Silica Sand No. 7, with an average particle size of 0.14 mm, was used as the ground material. It was compacted via free-fall to achieve relative densities $D_r$ of 50% and 90%, with model tests conducted for both cases. Sand was also placed inside the turbine's cylindrical pipe to match the internal ground level with the surrounding surface. Following ground preparation, water was infiltrated from the bottom of the container to submerge the model.

In the centrifuge tests, wind, wave, and seismic forces were applied sequentially—individually or in combination—in the same direction (left to right in the figure), while centrifugal acceleration of 50$g$ was imposed at the seabed surface. This paper reports results from three test conditions: (i) earthquake only, (ii) combined wind and waves, and (iii) combined wind, waves, and earthquake. Scaled to prototype equivalents, the earthquake corresponded to 1 Hz sine waves with 0.9 m/s$^2$ acceleration; wind speeds averaged 6.0–6.4 m/s (for $D_r$ = 50% case) and 5.0–5.1 m/s (for $D_r$ = 90% case); wave conditions reflected a plate amplitude of ±1.5 m (yielding ~2.2 m wave at the turbine) and a period of 7.14 s. Although these inputs did not represent extreme events capable of structural failure, the turbine exhibited pronounced vibration.

# 5 TEST RESULTS AND DISCUSSIONS

## 5.1 Lateral displacement and loading on tower and foundation pile

Strain gauges were affixed to an aluminium pipe simulating the pile to measure bending strain. Using this strain and the bending stiffness $EI$ of the pipe, the applied force was estimated via second-order differentiation with respect to depth, while horizontal displacement was obtained through second-order integration. The applied force refers to the resultant load acting on the pipe, comprising aerodynamic, wave, subgrade reaction, and inertial forces. As measurements were taken at discrete 20 mm intervals (equivalent to 1 m at the prototype scale), direct differentiation and integration introduced significant variability. To mitigate this, cubic $B$-spline

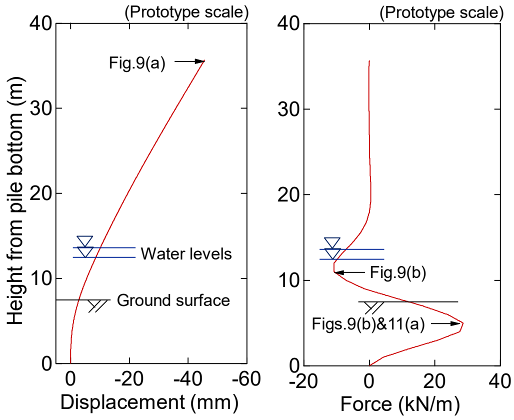


*Figure 7. Vertical distribution of horizontal displacement and applied force on pile at $D_r$=50% case (positive in windward direction).*

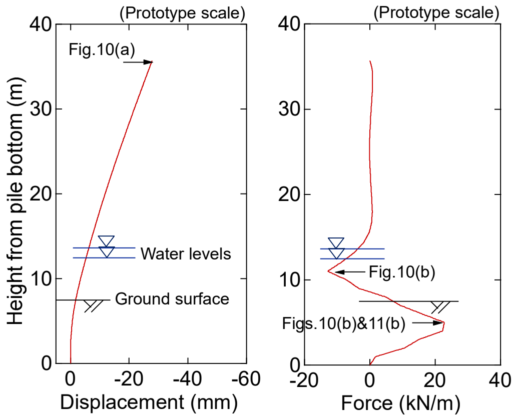


*Figure 8. Vertical distribution of horizontal displacement and applied force on pile at $D_r$=90% case (positive in windward direction).*

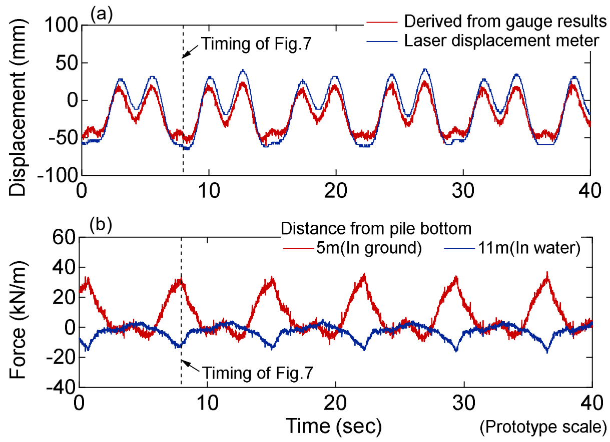


*Figure 9. Time histories of horizontal displacement and applied force on pile at $D_r$=50% case (positive in windward direction)*

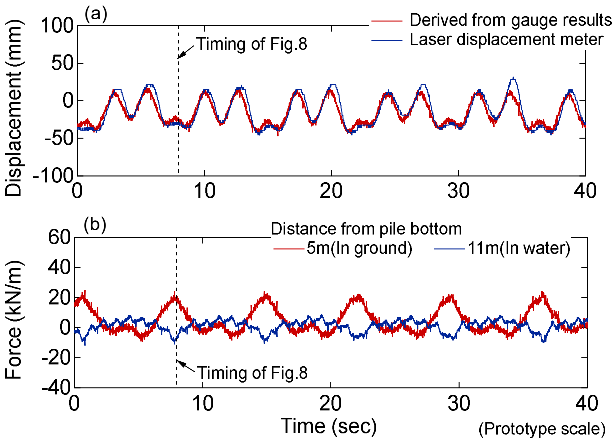


*Figure 10. Time histories of horizontal displacement and applied force on pile at $D_r$=90% case (positive in windward direction)*

interpolation was applied to smooth the data prior to analysis.

Figures 7 and 8 show the prototype horizontal displacement and applied force distribution (at peak wave loading) under combined wind and wave conditions (ii). For $D_r$ = 50%, Figure 7 indicates horizontal displacements of 45.0 mm at the tower top and 2.9 mm at ground level. Given a tower height of ~30 m, these correspond to displacement ratios of 0.15% and 0.01%, respectively. Dividing the 2.9 mm ground-level displacement by the 7.5 m embedment depth yields 0.04%, suggesting minimal ground plasticity. The vertical force distribution reveals opposing forces in the water and ground. Although not directly visible in the distribution, the thrust force on the nacelle was estimated at ~4 kN from the bending moment at the water surface prior to wave impact. These results confirm that the pile deflected under thrust and wave forces in the water, counteracted by subgrade reaction force.

In the $D_r$ = 90% case shown in Figure 8, horizontal displacement was smaller than in the $D_r$ = 50% case. The wind speed was ~20% lower, adjusted to maintain a similar rotor speed. Based on the bending moment at the water surface prior to wave incidence, the thrust force was estimated at ~3 kN, less than in the $D_r$ = 50% case. This adjustment introduced initial deflection differences at wind onset, likely influencing the results. Nonetheless, as discussed later, wave-induced displacement variation was also smaller in the $D_r$ = 90% case, indicating that increased ground density reduced tower displacement. The vertical distribution of applied forces again revealed opposing forces in the water and ground layers.

Figures 9 and 10 present the time histories of horizontal displacement and applied forces at the heights marked in Figures 7 and 8, shown at the prototype scale. For displacement, both strain gauge-derived values and laser displacement measurements are superimposed, confirming comparable magnitudes. The timing corresponds to the vertical distributions in Figures 7 and 8. At this moment, wave forces were

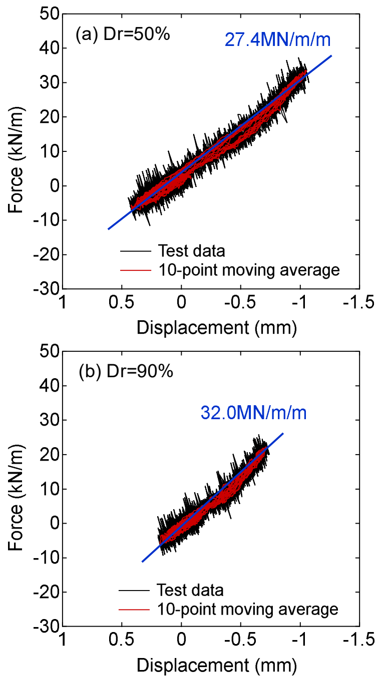


*Figure 11. Relationship between horizontal displacement and force.*

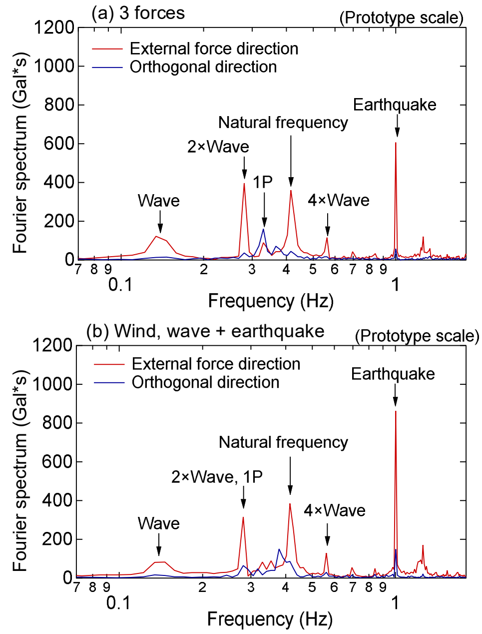


*Figure 12. Fourier spectrum of nacelle acceleration at $D_r$=50% case.*

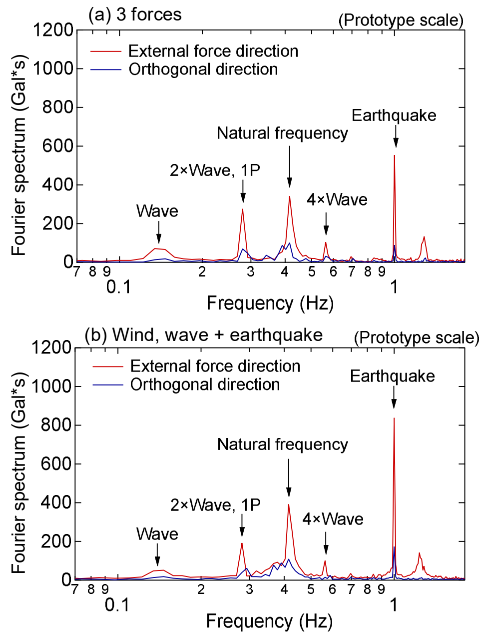


*Figure 13. Fourier spectrum of nacelle acceleration at $D_r$=90% case.*

greater on the leeward side, while subgrade reaction forces were larger on the windward side. In the opposite phase, both forces diminished.

Figure 11 shows the relationship between horizontal displacement and force at the indicated ground height marked in Figures 7 and 8, for $D_r$ = 50% and 90%, respectively. A moving average is included to reduce noise. When the displacement time history was differentiated twice, no discernible waveform remained, indicating negligible acceleration. This reflects the long-period, small-amplitude nature of wave-induced tower vibrations. Inertial forces were negligible, and the figure effectively represents the relationship between subgrade reaction force and tower displacement. In all cases, horizontal displacement was accompanied by force generation, confirming the presence of subgrade reaction. As large displacements did not occur, nonlinearity was minimal. Comparing the absolute gradients, the 90% case was 17% steeper than the 50% case, confirming that increased density enhances ground stiffness.

## 5.2 Nacelle vibration characteristics under combined external forces

The vibration characteristics of the nacelle are now examined. The developed simulator enables application of arbitrary wind, wave, and seismic forces, allowing model tests under diverse external loading conditions. As an example, two types of acceleration Fourier spectra are compared in Figures 12 and 13, showing spectral components in two directions: parallel and perpendicular to the direction of wind, wave, and seismic forces. All values are converted to prototype equivalents. Spectra in (a) corresponds to the simultaneous application of all three forces—(iii) wind, waves, and earthquake—while (b) represents the sum of spectra from (i) earthquake alone and (ii) combined wind and wave loading. In this paper, only the acceleration spectra are presented due to space limitations. However, velocity and displacement can be inferred from the acceleration and frequency, and the differences between the spectra reflect those in velocity and displacement.

Figures 12(a) and 13(a) indicate that vibrations predominantly occur in the direction of external forces. Distinct peaks appear at 0.14, 0.28, 0.33, 0.42, 0.56, and 1.0 Hz. The 0.14 Hz peak corresponds to the wave frequency, with 0.28 and 0.56 Hz as its harmonics. The 0.33 Hz peak in Figure 12(a) aligns with the rotor speed and represents a 1P vibration. In Figure 13(a), this frequency overlaps with the wave's second harmonic, rendering the 0.33 Hz peak indistinct. The 0.42 Hz peak corresponds to the first-mode natural frequency, while the 1.0 Hz peak is attributed to seismic excitation. Independent application of each external force confirmed that these vibrations arise separately. Although 3P vibrations—three times the rotor speed—are common in wind turbines, they were minor in this study. Under wind-only loading, a 3P vibration of ~14 Gal·s was observed, but remained small due to the short, wide blade geometry used, which differs from typical turbine designs.

Comparing Figures 12(b) and 13(b) with (a), the spectra show reduced amplitudes below the natural frequency and increased amplitudes above it. The cause remains unclear, but the results suggest that vibrations under combined loading are not strictly additive. In reality, wind turbines are subjected to simultaneous wind, wave, and seismic forces as in (a), yet current Japanese design guidelines (Exploratory Committee for Offshore Wind Power Facilities, 2020) adopt a methodology akin to (b). The validity of this approach warrants further verification. Moreover, discrepancies between the two cases may be amplified by phase differences and ground nonlinearity, underscoring the need for more detailed investigation.

## 6 CONCLUSIONS

This paper presents the development of a simulator capable of generating wind, wave, and seismic forces, along with model tests on fixed-bottom offshore wind turbines. It also reviews similarity laws for centrifuge testing. The simulator produced horizontal displacement and vibration in turbine models under combined loading, and different ground conditions were examined to assess their effects. The model tests showed that horizontal displacement produced soil reaction forces, though both were too small to reveal clear nonlinearity. Differences in ground stiffness were nevertheless evident. Nacelle acceleration analysis further indicated that the response under simultaneous three-force loading differed from the simple superposition of vibrations from force applied separately. Future work will expand testing conditions to further investigate turbine response to multiple external forces.

## ACKNOWLEDGEMENTS

This research was commissioned by the Ports and Harbours Bureau, Ministry of Land, Infrastructure, Transport and Tourism, Japan. Partial support was also provided by JSPS KAKENHI Grant Number JP24K07673. The authors gratefully acknowledge this support.

## REFERENCES

Arikawa, T. ed. (2024). Theory and Application of Hydraulic Modeling -Interaction between Fluid and Ground under Water Waves-. CRC Press, 236p. https://doi.org/10.1201/9781003424758

Baba, S., Miyake, M., Tsurugasaki, K., and Kim, H. (2002). Development of wave generation system in a drum centrifuge. *Proceedings of the International Conference on Physical Modelling in Geotechnics*, 265-270.

Exploratory Committee for Offshore Wind Power Facilities. (2020). Unified commentary on technical standards for offshore wind power facilities (translated by the authors). Ministry of Economy, Trade and Industry (METI) and Ministry of Land, Infrastructure, Transport and Tourism (MLIT), 184p. (in Japanese)

Sekiguchi, H. and Phillips, R. (1991). Generation of water waves in a drum centrifuge. *Proceedings of the International Conference CENTRIFUGE 91*, 343-350.

Takahashi, H., Fujii, N., Morikawa, Y. and Takano, D. (2019). Development of hydro-geotechnical centrifuge PARI Mark II-R. *Technical Note of the Port and Airport Research Institute*, No. 1353, 27p.

Takahashi, H., Morikawa, Y., and Kashima, H. (2019). Centrifuge modelling of breaking waves and seashore ground. *International Journal of Physical Modelling in Geotechnics*, 19(3): 115-127. https://doi.org/10.1680/jphmg.17.00037

Takahashi, H., Tsuchida, T., Kashima, H., Ohya, Y., Kurihara, O., and Ichikawa, T. (2025). Centrifuge model testing of fixed-bottom offshore wind turbines under combined wind, wave, and seismic loading. *Japanese Journal of JSCE*, 81(18): 25-18047, 7p. (in Japanese)

Takahashi, H., Zdravković, L., Tsiampousi, A., and Mori, N. (2022). Destabilisation of seawall ground by ocean waves. *Géotechnique*, 74(8): 713-728. https://doi.org/10.1680/jgeot.21.00420

Taylor, R.N. (1995). Geotechnical Centrifuge Technology. CRC Press, 296p. https://doi.org/10.1201/9781482269321

Wang, L. and Ishihara, T. (2024). Failure-mechanism for wind turbines supported by pile groups at the Kugino wind farm in the Kumamoto earthquake. *Structures*, 69: 20p. https://doi.org/10.1016/j.istruc.2024.107201

Yang,Y., Bashir, M., Li, C., Michailides, C., and Wang, J. (2020). Mitigation of coupled wind-wave-earthquake responses of a 10 MW fixed-bottom offshore wind turbine. *Renewable Energy*, 157: 1171-1184. https://doi.org/10.1016/j.renene.2020.05.077